Iron nanoparticles supported ordered mesoporous CeO₂, an efficient catalyst for photo-Fenton oxidation of phenol under irradiation

Zahra Bailiche[1,2] · Amina Berrichi[1,2] · Redouane Bachir[1]

Abstract

Mesoporous CeO_2-supported iron nanoparticles were prepared by the hard template method with different iron loading. The catalysts were characterized by XRD, BET, UV–Vis, ICP, SEM–EDX, MET and TPR. The catalysts showed high activity and stability in the photo-Fenton oxidation of aqueous phenol solution using near-ultraviolet irradiation (254 nm) at room temperature and neutral pH. The catalytic performance has been monitored in terms of aromatics and total organic carbon (TOC), and phenol conversion. Also, a comparative study between the CeO_2 activity and catalysts was monitored which demonstrates that iron has a synergistic effect in the phenol photo-Fenton oxidation. Moreover, the formation of OH· and O_2· radicals accelerates the process by reducing Fe^{3+} to Fe^{2+} and Ce^{4+} to Ce^{3+} which leads to a total phenol oxidation at short time process. The total phenol conversion was obtained at 15 min with $Fe/CeO_2(60)$ and 20 min with $Fe/CeO_2(20)$.

Keywords Photo-Fenton · Phenol · Oxidation · Fe · CeO_2 · Nanoparticles · H_2O_2

Introduction

The development and application of several advanced oxidation processes (AOPs) to water treatment have been significant research in environmental reaction engineering during the last decades [1]. The Fenton process has been proposed for degrading organic pollutants using different catalysts [2]. Fenton oxidation using an heterogeneous catalyst is an efficient method for pollutant degradation; moreover, several catalytic systems were utilized, such as Fe-based MOF materials which used for the

✉ Amina Berrichi
    amina.berrichi@univ-temouchent.edu.dz; berrichi.amina@yahoo.fr

1   Laboratory of Catalysis and Synthesis in Organic Chemistry, University of Tlemcen, BP 119, 13000 Tlemcen, Algeria

2   Faculty of Science, University of Ain Temouchent, BP 284, 46000 Ain Temouchent, Algeria

degradation of methylene blue[3], iron oxide nanoparticles has been reported for the paracetamol degradation [4] and MIL-100(Fe) metal–organic framework which demonstrated a high performance for total phenol oxidation [5]. These catalysts could rapidly generate Fe^{2+} and hydroxyl radical-based Fenton oxidation.

Phenol and its derivatives are the most dangerous organic pollutants, with high concentrations that can damage our life and human, where it is necessary for their degradation and elimination [6]. For this purpose, several groups reported phenol degradation by iron catalysts. The Fe/SBA-15 catalyst was used successfully in the photo-Fenton degradation of phenol by H_2O_2 with a total conversion at 10 min [7]; also, this one was used under near UV–Vis irradiation at room temperature and gave good results [8].

The mesoporous materials are known by the high surface area, large pore volume and well defined pore size, making it a potential material in catalysis, adsorption, organic synthesis [9] and other fields [10, 11]. CeO_2 is a typical rare earth oxide which has an oxygen storage capacity, and it is often used as support material for catalysts reactions, the excellent catalytic activity is attributed to the presence of oxygen vacancies on the oxide surface and the ability of surface Ce^{3+} at such defect sites to preserve its fluorite structure [12]. Moreover, the doping of CeO_2 by iron leads to the formation of stable redox couple of cerium (Ce^{4+}/Ce^{3+}) and iron (Fe^{3+}/Fe^{2+}) cations which demonstrate a high performance during waste water treatment against organic dyes [13]. This catalyst has been used in several processes such as photocatalytic ozonation [14], methylene blue degradation where the redox cycle between Fe^{3+}/Ce^{4+} and Fe^{2+}/Ce^{3+} was accelerated by the oxygen defects [15], and Tetracycline degradation [16]. Also, mesoporous Co_3O_4/CeO_2 was reported for the phenol Fenton oxidation using peroxymonosulfate as activator with a total phenol degradation for 50 min [17].

The mesoporous CeO_2 material was prepared by different methods such as sol–gel, precipitation, and hard template. With this one, researchers used mesoporous silica KIT-6 [18, 19] and SBA-15 [20] as a template to obtain an ordered and structure. The aim of our research is find a key to eliminate dyes and water treatment using simple process in mild reaction condition and reduced time avoiding contamination. In this paper, the mesoporous Fe/CeO_2 was prepared by the hard template and impregnation method for iron doping with two different molar ratio of Ce/Fe equal to 60 and 20. The catalysts activity was performed in phenol degradation in an aqueous solution by the photo-Fenton process.

Experimental

Reagent

All reagents were purchased from Sigma-Aldrich. Tetraethyl-orthosilicate, amphiphilic triblock copolymer poly (ethylene oxide)-poly(propylene oxide)-poly(ethylene oxide) average molecular weight 5800.

Preparation of mesoporous Fe/CeO$_2$

Firstly, the mesoporous SBA-15 were synthesized with the same preparation reported by Zhao et al. [21, 22], 4 g of amphiphilic triblock copolymer poly(ethylene oxide)-poly(propylene oxide)-poly(ethylene oxide) was mixed in 120 g of water and 8.64 g of 2 M HCl solution at 40 °C while stirring, followed by adding 8.54 g of tetraethyl-orthosilicate to the homogenous solution under stirring for 24 h. For crystallization, this gel mixture was finally put in a Teflon-lined autoclave for 2 days at 100 °C. After cooling to room temperature, the solid product was filtered and dried in the air at room temperature; Template removal was achieved by calcination in air at 500 °C for 4 h (heating rate: 1 °C/mn). Then, mesoporous ceria was synthesized according to the following procedure developed by Yue and Zhou [20]. One mmole of Ce(NO$_3$)$_3$.6H$_2$O was mixed with 0,15 g of mesoporous silica and was ground for a few minutes. The mixture was then put into a crucible and placed in a muffle furnace. The temperature was increased from room temperature to 500 °C with a rate of 1 °C/min and maintained at the final temperature for 4 h. The specimen was then cooled down to room temperature. The silica template was removed by 2 M NaOH solution at 80 °C, and the porous ceria was recovered by centrifugation and washed with distilled water three times. The Fe/CeO$_2$ catalyst was prepared by impregnation method. The CeO$_2$ was dispersed in 50 mL of deionized water containing various ferric amounts, to obtain a well-defined Ce/Fe ratio equal to 20 and 60.

Photo-Fenton reaction

Heterogeneous photo-Fenton reactions were carried out in a cylindrical Pyrex reactor with one central and three peripheral female conical connections for the inflow and outflow of the solution model, under UV irradiation (254 nm) using phenol as reactant and hydrogen peroxide as oxidant. The catalyst (100 mg) was put into 100 mL of an aqueous phenol solution (5×10^{-4} mol L^{-1}), and the required amount of H$_2$O$_2$ was used for complete phenol oxidation.

$$C_6H_5OH + 14H_2O_2 \rightarrow 6CO_2 + 17H_2O$$
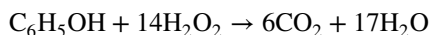
The reaction was carried out in ambient conditions (atmospheric pressure, 25 °C and neutral pH). Phenol conversions were determined by high-performance liquid chromatography (HPLC, waters 600) equipped with a C-18 column at a rate of 1 mL/min with UV detection with a mobile phase of 20% acetonitrile and 80% H$_2$O.

Characterization method

Various techniques were used to determine the structure of the catalyst. Diffuse reflectance DRUV-Vis spectroscopy measurements using a Lambda 800 UV–Vis spectrometer in the range of 200–800 nm at room temperature.

N_2 adsorption, the BET surface areas were determined from N_2 adsorption isotherms at 77 K using a Quantachrom NOVA 1000 instrument. The catalyst was outgazed in situ at 250 °C for 10 h.

Powder X-rays diffraction (XRD) patterns were collected using an Ultima III Rigaku Monochromatic Diffractometer using Cu Kα radiation ($\lambda = 1.5406$ A°) with a rate of 1°/min in the 2θ range 20–80°.

The temperature-programmed reduction experiments (TPR) were carried out in an Altamira AMI-200 apparatus with 5% H_2/Ar flow (30 mL/min) with a rate of 5 °C/min at 800 °C.

Transmission electron microscopy (TEM) micrographs were collected on a JEOL JEM-1230 electron microscope. All samples were dispersed in ethanol and sonicated for 20 min.

Iron leaching and the amount were systematically evaluated by ICP (induced coupled plasma) analyses model (820 MS Varian). After the reaction, the total organic carbon (TOC) content was analyzed using a Shimadzu TOC-VCSH analyzer.

Results and discussion

Catalyst characterization

The XRD analysis on each pattern demonstrates that the diffraction peaks were perfectly indexed to a face-centered cubic (fcc) fluorite structure of CeO_2 (JCDS card N°34-0394). The broad peaks suggested the presence of small CeO_2 crystallites (Fig. 1). Compared with the diffraction of pure mesoporous CeO_2, the XRD pattern of Fe/CeO_2 is similar to pure CeO_2. No XRD diffraction peaks of iron oxide are observed due to its low content. Also, the molar ratio of Ce/Fe does not affect the spectra.
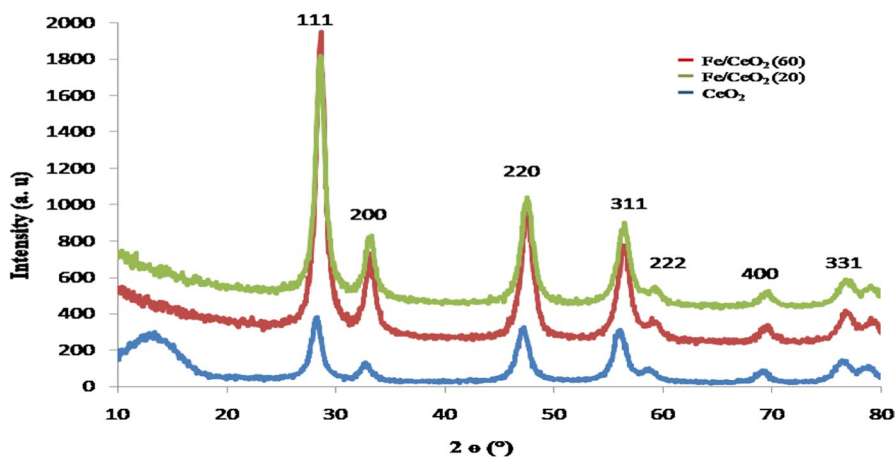
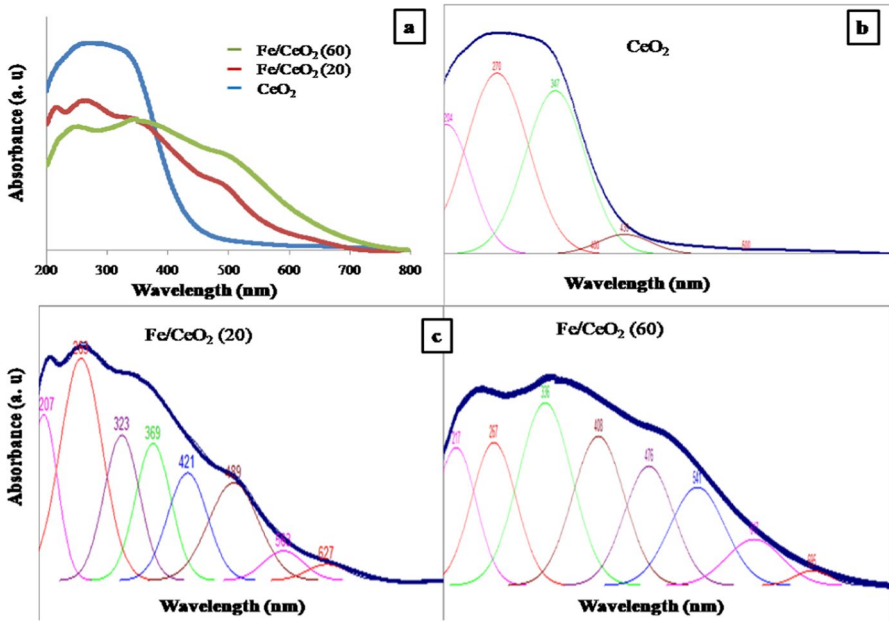

Fig. 1 XRD patterns for CeO_2 and Fe/CeO_2

Fig. 2 UV–Vis diffuse reflectance spectra of **a** CeO$_2$ and Fe/CeO$_2$, **b** CeO$_2$ deconvolution spectrum and **c** deconvolution spectra of Fe/CeO$_2$

To identify the nature of the iron species, the catalysts were analyzed by UV–visible (Fig. 2a). The deconvolution of the UV–visible spectrum of CeO$_2$ (Fig. 2b) demonstrates bands at 203 nm, 270 nm, 347 and 438 nm corresponding to the charge transfer of O^{2-} to Ce^{4+} and the charge transfer of oxygen to cation species in a lower oxidative state, respectively [11]. The spectra of Fe/CeO$_2$(20) and Fe/CeO$_2$(60) show new bands (Fig. 2c), the displacement of these bands is shown in Table 1. In the first one, new bands were situated at 322 nm, which shifted to a higher wavelength from Fe/CeO$_2$(60) to 407 nm. The band located at 322 nm characterized the isolated Fe^{3+} in tetrahedral coordination sites [23]. In addition, the band shift is due

Table 1 DRUV–Vis bands shift of the CeO$_2$, Fe/CeO$_2$(20), and Fe/CeO$_2$(60)

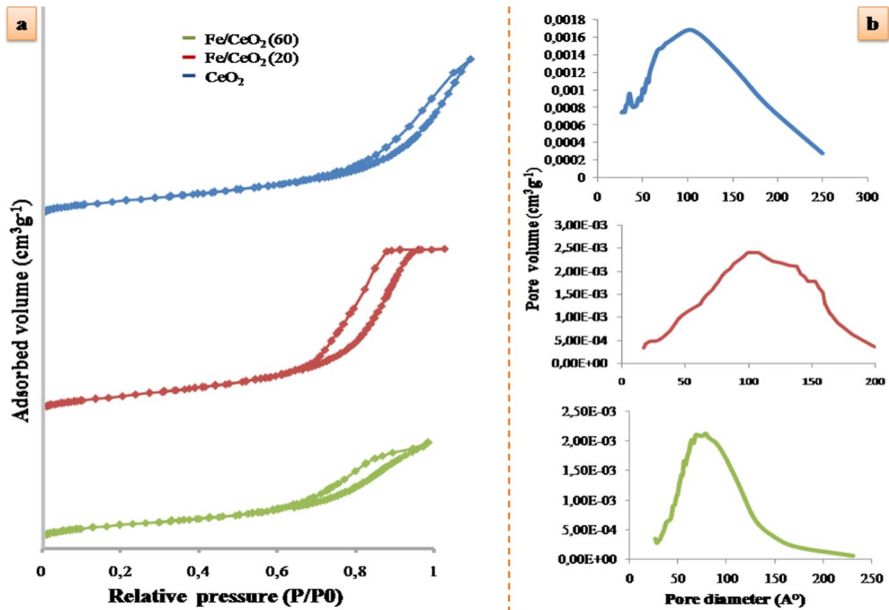| CeO$_2$	Fe/CeO$_2$(20)	Fe/CeO$_2$(60)
203	206	216
270	262	267
347	369	336
438	489	407
	323	475
	420	540
	562	617
	627	695

Fig. 3 **a** N_2 adsorption–desorption isotherms and **b** pore size distributions of CeO_2 and Fe/CeO_2 catalysts measured at 77 K

Table 2 Textural properties of the prepared catalysts	Catalyst	S_{BET} (m^2/g)	V_T (m^3/g)	Pore diameter (A°)
	CeO_2	118,30	0,27	96,40
	Fe/CeO_2(20)	106.32	0.33	91.87
	Fe/CeO_2(60)	98.18	0.33	91.30

to the interaction between CeO_2 and iron nanoparticles. Other new bands situated at 489, 552, and 627 nm for Fe/CeO_2(20) attributed to Fe_2O_3 clusters [24]; these bands were shifted 54, 617, and 695 nm to in the case of Fe/CeO_2(60).

Figure 3 demonstrates the N_2 adsorption–desorption isotherms of CeO_2Fe/CeO_2(20) and Fe/CeO_2(60) catalysts. The structural properties of the support and catalyst samples are listed in Table 2. The isotherms are identified as type IV according to the IUPAC classification with is a typical characteristic of mesoporous material. After loading iron, the shape of the isotherms of $FeCeO_2$ catalyst is similar to that of pure ceria; the BET surface area decreases with the increasing amount of iron which confirmed that iron nanoparticles were deposited and incorporated in the pore of CeO_2 support [25].

Figure 4 displays the H_2-TPR profile of CeO_2, Fe/CeO_2(20) and Fe/CeO_2(60). The H_2-TPR profile of CeO_2 demonstrates two peaks around 520 and 700 °C, which are assigned to the reduction in surface oxygen and bulk oxygen, respectively [26].
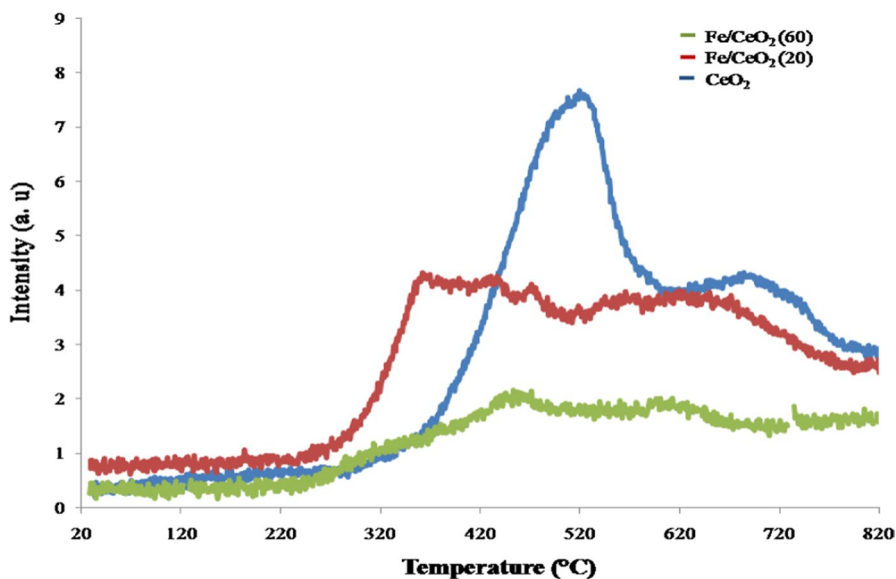
Fig. 4 H_2-TPR profile of CeO_2, $Fe/CeO_2(20)$ and $Fe/CeO_2(60)$

In the case of the supported catalyst with iron, these peaks were shifted to the lower temperature. Other shoulder peaks were also presented, situated at 420 °C with higher and lower iron content. This demonstrates FeO's presence by reducing Fe_2O_3 [27]. The first reduction of Fe_2O_3 to Fe_3O_4 is not presented in the profiles, which appear between 50 and 100 °C [28]. This result shows that the oxidation state of iron is Fe^{2+} and Fe^{3+}.

TEM images are shown in Fig. 5. The image 5a demonstrates that CeO_2 has a mesoporous structure, and it takes the SBA-15 shape with an ordered structure and is very clear at 20 nm. For the $Fe/CeO_2(20)$, where the iron content is higher, the iron was deposited on the surface of the support with some iron accumulation, but decreasing the iron content in the catalyst $Fe/CeO_2(60)$, presented an excellent dispersion with small iron nanoparticles in the round of 5 nm.

The energy-dispersive X-ray spectroscopy (EDX) analysis of CeO_2 prepared by hard template (Fig. 5b) demonstrates the high presence of Ce and low content of Si, which does not exceed 1%.

Catalyst activity

For the phenol Fenton oxidation, the catalysts $Fe/CeO_2(20)$ and $Fe/CeO_2(60)$ were used at room temperature under ultraviolet irradiation at 250 nm with neutral pH. The conversion of phenol is shown in Fig. 6a. In $Fe/CeO_2(60)$ presence, 47% of phenol was degraded for 5 min and 95% for 10 min. The phenol was completely converted for 15 min. The $Fe/CeO_2(20)$ catalyst was more reactive for 5 min and 10 min; it gave high conversions of 70% and 93%, respectively. Also, it gave the
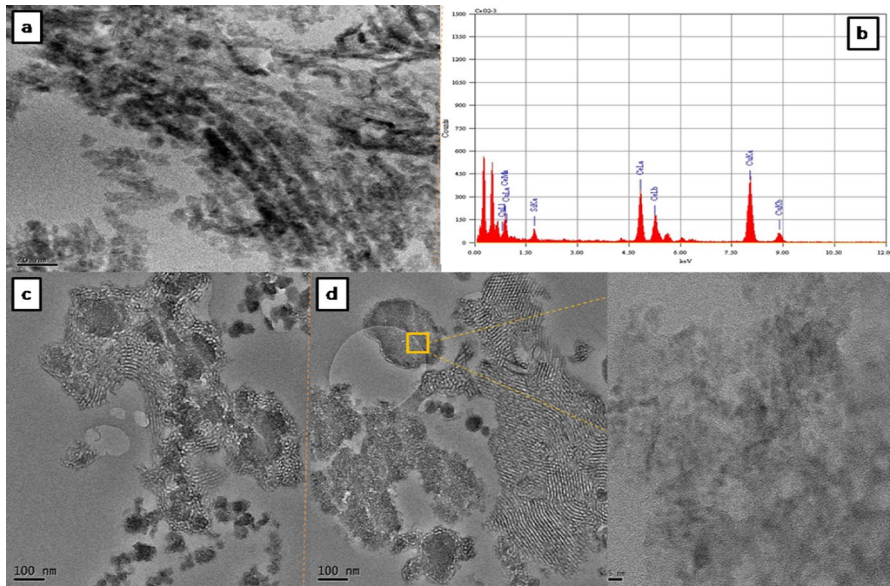
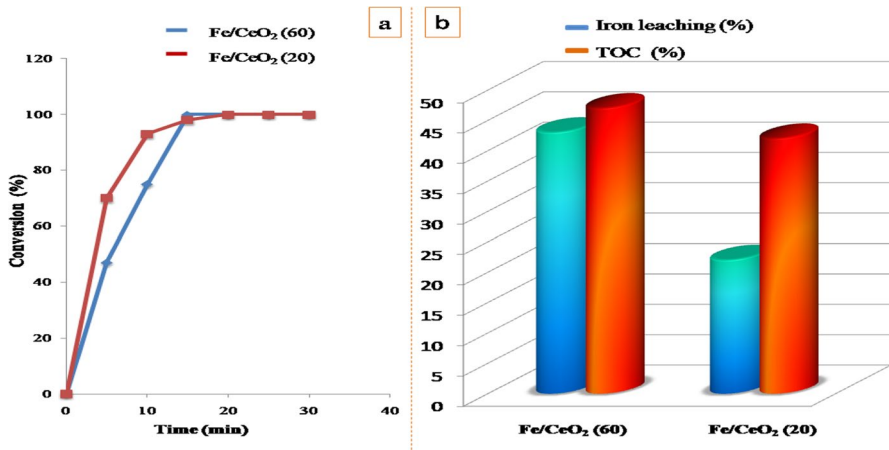**Fig. 5** TEM images of **a** CeO_2, **b** EDX analysis of CeO_2, **c** Fe/CeO_2(20) and **d** Fe/CeO_2(60)

Fig.6 **a** Photo-Fenton oxidation of phenol at 25 °C $\pm$ 1 °C, **b** TOC and iron leaching in the presence of Fe/CeO_2 catalysts

total degradation for 20 min. This result shows that the high loading of iron gives the total phenol degradation in a short time (15 min).

In addition, to quantify the phenol mineralization, total organic carbon (TOC) removals for the process are determined in Fig. 6b. For the Fe/CeO_2(60), 47% of removed TOC was achieved, while Fe/CeO_2(20) was used as a catalyst, 42% removal was obtained. The efficiency of the Fenton type process is influenced by the

concentration of Fe^{2+} ions and Ce^{4+}, which catalyze H_2O_2 decomposition resulting OH radical production and, consequently, the degradation of organic molecules.

The amount of iron leaching in the photo-Fenton degradation of phenol reaction is measured and presented in Fig. 6b. For $Fe/CeO_2(60)$ catalyst, 43% of iron loss. The amount of iron leaching decreased in the case of $Fe/CeO_2(20)$ to 22% loss.

To demonstrate the effect of iron on the active sites of CeO_2, this one was used in the reaction without metal. The activity of CeO_2 increases with reaction time giving a total phenol conversion at 15 min. After iron deposition, the conversion increases with $Fe/CeO_2(20)$ to 70% at 5 min. This result confirms that iron has a synergistic effect and the presence of oxygene vacancies reduces Fe^{3+}/Ce^{4+} to Fe^{2+}/Ce^{3+} producing more OH· radicals which accelerate the process. The stability of catalysts was studied after the first reaction run; the catalysts were washed with water and dried without any treatment. The reusability of $Fe/CeO_2(20)$ and $Fe/CeO_2(60)$ in the photo-Fenton oxidation of phenol is demonstrated in Table 3. For the first cycle, the decrease in Ce/Fe from 60 to 20 accelerates the oxidation of phenol, producing more radicals with higher iron-loaded catalyst ($Fe/CeO_2(20)$). In the second run of the reaction, the $Fe/CeO_2(20)$ and $Fe/CeO_2(60)$ demonstrate high activity than the first one at 10 min and give phenol conversion equal to 96 and 100%, respectively. In the first cycle, the iron leaching was more intense in the case of $Fe/CeO_2(60)$ than $Fe/CeO_2(20)$, where the activity of the same catalyst was more pronounced in the second run with total phenol oxidation at 10 min (Table 3). Also, it is the same effect on the $Fe/CeO_2(20)$ activity where total phenol oxidation achieved at 15 min for the second run. This result demonstrates that the iron leaching exposed the Ce^{4+} and Ce^{3+} active sites and shows the easy redox cycle between Ce^{3+} and Ce^{4+}, which is an oxygen buffer to produce OH· radical in the case of $Fe/CeO_2(60)$ [19].

Iron nanoparticles supported ordered mesoporous CeO_2 catalyst demonstrates a high performance for the phenol photo-Fenton oxidation process in the presence of H_2O_2. This capacity due to the formation of oxygene and OH· radicals which are known in photocatalysis using oxid support such as TiO_2 and CeO_2 [29]. The O_2· and OH· can produce during the reaction mechanism in the presence of irradiation (Fig. 7). Firstly, the UV irradiation of catalyst provoke the electron (e^-) movement on band valance to the conduction band leaving h^+ (Eqs. 1). Then, in the presence of H_2O_2, O_2 vacancies and OH· were formed by reduction of Fe^{3+} to Fe^{2+} and Ce^{4+} to Ce^{3+} [Eqs. (2)–(5)] giving HO_2 as

Table 3 Stability of $Fe/CeO_2(20)$ and $Fe/CeO_2(60)$ catalysts

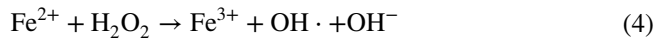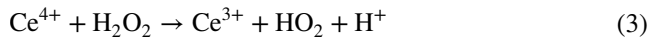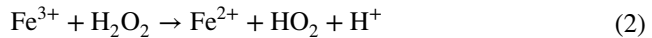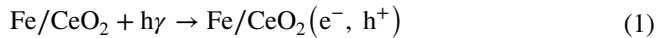| Catalyst	$Fe/CeO_2(20)$		$Fe/CeO_2(60)$		CeO_2
Reaction time (min)	Conv. (%) cycle 1	Conv. (%) cycle 2	Conv. (%) cycle 1	Conv. (%) cycle 2	Conv. (%) cycle 1
0	0	0	0	0	0
5	70	90	47	91	50
10	93	96	95	100	80
15	98	100	100	100	100
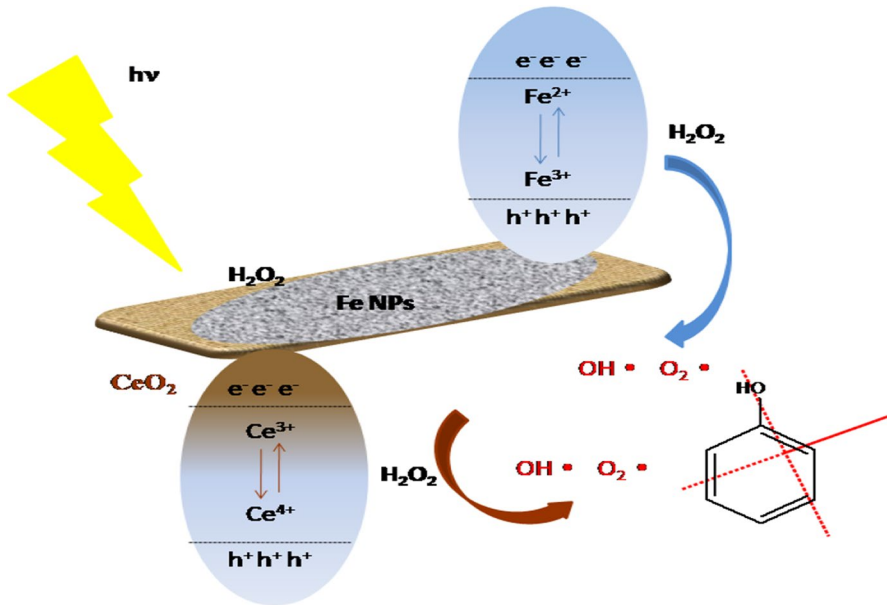
Fig.7 Possible phenol photo-Fenton oxidation process mechanism using Fe/CeO$_2$ catalyst

intermediates. The present radicals attack directly the phenol molecule to produce CO_2 and H_2O [15, 30]. The synergistic effect between the oxygene vacancies and OH· formed by Fe^{3+}/Fe^{2+} and Ce^{4+}/Ce^{3+} activates the photo-Fenton process.

$$Fe/CeO_2 + h\gamma \rightarrow Fe/CeO_2\left(e^-, h^+\right) \tag{1}$$

$$Fe^{3+} + H_2O_2 \rightarrow Fe^{2+} + HO_2 + H^+ \tag{2}$$

$$Ce^{4+} + H_2O_2 \rightarrow Ce^{3+} + HO_2 + H^+ \tag{3}$$

$$Fe^{2+} + H_2O_2 \rightarrow Fe^{3+} + OH \cdot + OH^- \tag{4}$$

$$Ce^{3+} + H_2O_2 \rightarrow Ce^{4+} + OH \cdot + OH^- \tag{5}$$

$$Fe^{3+} + HO_2 \rightarrow Fe^{2+} + O_2 \cdot + H^+ \tag{6}$$

$$Ce^{4+} + HO_2 \rightarrow Ce^{3+} + O_2 \cdot + H^+ \tag{7}$$
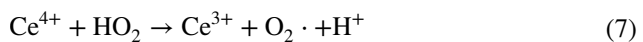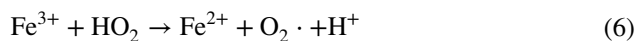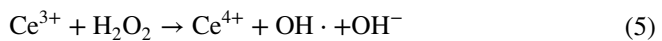
Conclusion

In the present study, it has been demonstrated that iron-supported ordered mesoporous CeO$_2$ is an efficient catalyst for the total oxidation of phenol through the photo-Fenton process for 15 min under UV. Also, the effect of the Ce/Fe ratio was studied using 20 and 60. This part achieved that the catalyst with high iron content activates the photo-Fenton process by the synergistic between iron and CeO$_2$ and gives the total phenol conversion. Furthermore, the leaching of iron study demonstrates that the catalyst with high leaching provides high activity in the second run due to the abundant oxygen vacancies and Ce^{3+}, which are more exposed on the surface of the catalyst; this suggested directly related to the amount of redox active Ce^{3+} sites at the surface. Finally, the photo-Fenton process can be influenced by the metal content, surface area, and metal leaching.

Availability of data and materials All of the material is owned by the authors and/or no permissions are required and it is available.

Declarations

Conflict of interest The author declared that there is no conflict of interest.

Ethical approval I have read and understood the publishing policy, and submit this manuscript in accordance with this policy.

Consent to participate I have read and understood the publishing policy, and submit this manuscript in accordance with this policy.

Consent for publication I am Berrichi Amina, I give my consent for the publication of identifiable details, which can include material, figures which to be published in Cellulose Journal. I confirm that I have seen and been given the opportunity to read both the material and the article as attached to be published by this journal. I have discussed this consent form authors.

References

1. S. Esplugas, J. Gimenez, S. Contreras, E. Pascual, M. Rodríguez, Water Res. **36**, 1034 (2002)
2. B. Jain, A.K. Singh, H. Kim, E. Lichtfouse, V.K. Sharma, Environ. Chem. Lett. **16**, 947 (2018)
3. F. Martínez, P. Leo, G. Orcajo, M. Díaz-García, M. Sanchez-Sanchez, G. Calleja, Catal. Today **313**, 6 (2018)
4. F. Velichkova, C. Julcour-Lebigue, B. Koumanova, H. Delmas, J. Environ. Chem. Eng. **1**, 1214 (2013)
5. D. Ozer, O. Icten, N. Altuntas-Oztas, B. Zumreoglu-Karan, Res. Chem. Intermed. **46**, 909 (2020)
6. A.M. Al-Hamdi, M. Sillanpää, J. Dutta, Res. Chem. Intermed. **42**, 3055 (2016)

7. Z. Bailiche, L. Cherif, S. Royer, A. Bengueddach, S. Fourmentin, S. Siffert, Heterogeneous advanced photo-Fenton oxidation of phenolic aqueous solutions over iron-containing SBA-15 catalyst, in *MATEC Web of Conferences* (EDP Sciences, 2013), pp. 04033
8. F. Martínez, G. Calleja, J. Melero, R. Molina, Appl. Catal. B Environ. **60**, 181 (2005)
9. M.E.A. Drici, B. Amina, B. Redouane, B. Mohammed, B. Sumeya, M. Debdab, React. Kinet. Mech. Catal. **136**, 333 (2023)
10. S.P. Ghuge, A.K. Saroha, J. Environ. Manag. **211**, 83 (2018)
11. A. Berrichi, R. Bachir, S. Bedrane, N. Choukchou-Braham, K. Belkacemi, Res. Chem. Intermed. **45**, 3481 (2019)
12. H. Wang, S. Luo, M. Zhang, W. Liu, X. Wu, S. Liu, J. Catal. **368**, 365 (2018)
13. M.M. Khan, R. Siwach, S. Kumar, M. Ahamed, J. Ahmed, J. Alloy. Compd. **856**, 158127 (2021)
14. S. Xu, X. Chen, S. Zhan, S. Tian, Y. Xiong, J. Chem. Technol. Biotechnol. **96**, 1523 (2021)
15. S.S. Gc, K. Alkanad, A. Hezam, A. Alsalme, N. Al-Zaqri, N. Lokanath, J. Mol. Liq. **335**, 116186 (2021)
16. L. Niu, G. Zhang, G. Xian, Z. Ren, T. Wei, Q. Li, Y. Zhang, Z. Zou, Sep. Purif. Technol. **259**, 118156 (2021)
17. Q. Gao, Y. Cui, S. Wang, B. Liu, C. Liu, Environ. Sci. Pollut. Res. **28**, 27852 (2021)
18. X. Zhang, D. Wang, M. Jing, J. Liu, Z. Zhao, G. Xu, W. Song, Y. Wei, Y. Sun, ChemCatChem **11**, 2089 (2019)
19. K. Li, Y. Zhao, C. Song, X. Guo, Appl. Surf. Sci. **425**, 526 (2017)
20. H.-M. Zhao, C.-M. Di, L. Wang, Y. Chun, Q.-H. Xu, Microporous Mesoporous Mater. **208**, 98 (2015)
21. D. Zhao, J. Feng, Q. Huo, N. Melosh, G.H. Fredrickson, B.F. Chmelka, G.D. Stucky, Science **279**, 548 (1998)
22. A. Berrichi, Z. Bailiche, R. Bachir, Res. Chem. Intermed. **48**, 4119 (2022)
23. Y. Wang, S. Lkhamjav, B. Qiu, C. Dong, C. Dong, Y. Zhou, B. Shen, M. Xing, J. Zhang, Res. Chem. Intermed. **43**, 2055 (2017)
24. M.S. Kumar, M. Schwidder, W. Grünert, A. Brückner, J. Catal. **227**, 384 (2004)
25. V. Popkov, V. Tolstoy, S. Omarov, V. Nevedomskiy, Appl. Surf. Sci. **473**, 313 (2019)
26. S. Watanabe, X. Ma, C. Song, J. Phys. Chem. C **113**, 14249 (2009)
27. H. Lan, J. Zeng, B. Zhang, Y. Jiang, Res. Chem. Intermed. **45**, 1565 (2019)
28. H.-Y. Lin, Y.-W. Chen, C. Li, Thermochim. Acta **400**, 61 (2003)
29. E. Richards, D. Murphy, M. Che, Res. Chem. Intermed. **45**, 5763 (2019)
30. J.T. Hernández-Oloño, A. Infantes-Molina, D. Vargas-Hernández, D.G. Domínguez-Talamantes, E. Rodríguez-Castellón, J.R. Herrera-Urbina, J.C. Tánori-Córdova, J. Photochem. Photobiol. A Chem. **421**, 113529 (2021)